

## All-transfer electrode interface engineering towards harsh-environment-resistant MoS<sub>2</sub> field-effect transistors

*Yonghuang Wu, Zeqin Xin, Zhibin Zhang, Bolun Wang, Ruixuan Peng, Enze Wang, Run Shi, Yiqun Liu, Jing Guo, Kaihui Liu, Kai Liu\**

Y. H. Wu, Z. Q. Xin, B. L. Wang, R. X. Peng, E. Z. Wang, R. Shi, Y. Q. Liu, J. Guo and Prof. K. Liu

State Key Laboratory of New Ceramics and Fine Processing

School of Materials Science and Engineering, Tsinghua University

Beijing 100084, China

E-mail: [liuk@tsinghua.edu.cn](mailto:liuk@tsinghua.edu.cn)

Z. B. Zhang and Prof. K. H. Liu

State Key Laboratory for Mesoscopic Physics

Frontiers Science Center for Nano-optoelectronics

School of Physics, Peking University

Beijing 100871, China

Keywords: molybdenum disulfide, interface engineering, van der Waals electrodes, harsh-environment resistance, field-effect transistor

This article has been accepted for publication and undergone full peer review but has not been through the copyediting, typesetting, pagination and proofreading process, which may lead to differences between this version and the [Version of Record](#). Please cite this article as [doi: 10.1002/adma.202210735](https://doi.org/10.1002/adma.202210735).

This article is protected by copyright. All rights reserved.

**Abstract.** Nanoscale electronic devices that can work in harsh environments are in high demand for wearable, automotive, and aerospace electronics. Clean and defect-free interfaces are of vital importance for building nanoscale harsh-environment-resistant devices. However, current nanoscale devices are subject to failure in these environments, especially at defective electrode-channel interfaces. Here, we develop harsh-environment-resistant MoS<sub>2</sub> transistors by engineering electrode-channel interfaces with an all-transfer of van der Waals electrodes. The delivered defect-free, graphene-buffered electrodes keep the electrode-channel interfaces intact and robust. As a result, the as-fabricated MoS<sub>2</sub> devices have reduced Schottky barrier heights, leading to a very large on-state current and high carrier mobility. More importantly, the defect-free, hydrophobic graphene buffer layer prevents metal diffusion from the electrodes to MoS<sub>2</sub> and the intercalation of water molecules at the electrode-MoS<sub>2</sub> interfaces. This enables high resistances of MoS<sub>2</sub> devices with all-transfer electrodes to various harsh environments, including humid, oxidizing, and high-temperature environments, surpassing the devices with other kinds of electrodes. Our work deepens the understanding of the roles of electrode-channel interfaces in nanoscale devices and provides a promising interface engineering strategy to build nanoscale harsh-environment-resistant devices.

## 1. Introduction

As the semiconducting industry opens up the sub-10 nm node era, a further increase in circuit integration requires innovations of both materials and device configurations at the nanoscale.<sup>[1-3]</sup> Two-dimensional transition metal dichalcogenides (2D-TMDCs), owing to their low surface scattering of carriers and high mobility at the atomic thickness limit, have been regarded as promising channel materials beyond silicon to extend Moore's law.<sup>[4-6]</sup> In the past decade, a variety of TMDCs have been extensively explored for nanoelectronics. The electrode-TMDC interface is found to play a critical role in determining the electrical transport properties of TMDC devices.<sup>[7]</sup> However, the deposition of conventional metal electrodes could damage ultrathin TMDCs and introduce defects at the electrode-TMDC interface, resulting in Fermi level pinning (FLP) and high interface barriers.<sup>[8]</sup> In recent years, therefore, many strategies have been developed to decrease the barrier height and reduce the contact resistance between electrodes and TMDCs, including the use of low work function metal,<sup>[9,10]</sup> insertion of a buffer layer,<sup>[11-14]</sup> and transfer of metal electrodes.<sup>[15,16]</sup> These efforts have pushed TMDC devices more forward towards real applications.

In many real applications, however, highly integrated nanoscale electronic devices must also adapt to special environments. For wearable, automotive, and aerospace electronics, there are growing demands for highly integrated, harsh-environment-resistant electronic devices that can work

This article is protected by copyright. All rights reserved.

at high temperatures, at high humidity, or in oxidizing environments.<sup>[17-19]</sup> This creates many new challenges for nanoscale devices, especially for TMDC devices. Interestingly, nanoscale devices are subject to failure in these environments usually at the electrode-channel interfaces, rather than at the channels themselves. For example, low work-function metals used as buffer layers of electrodes in TMDC devices, such as Ti, In, and Bi, are susceptible to oxidation in air and even under high vacuum.<sup>[20]</sup> The oxidization of these metals and the induced defects of TMDCs due to metal deposition (**Figure 1a**) would become more severe at high temperatures,<sup>[21]</sup> resulting in poor stability of TMDC devices because metals may diffuse into and react with the defective TMDCs. In contrast, the transfer of metal electrodes has the electrode-TMDC interface less defective due to the formation of van der Waals (vdW) contact and is thus considered an effective approach to high-performance TMDC devices. However, in harsh environments, as molecules (such as water molecules in humid environments) may be intercalated into relatively large vdW gaps, the TMDC devices would be greatly degraded due to severe scattering of carriers and possible chemical reactions at the electrode-TMDC interface (Figure 1b). Therefore, the delicate design of electrode-TMDC interfaces is indispensable for harsh-environment-resistant TMDC devices, which requires the electrode-TMDC interfaces not only to have fewer defects but also to prevent metal diffusion and molecule intercalation.

In this work, we develop harsh-environment-resistant MoS<sub>2</sub> transistors by engineering electrode-MoS<sub>2</sub> interfaces with all-transfer Au/monolayer graphene (t-Au/graphene) electrodes. In our method, chemical-vapor-deposited (CVD) high-quality monolayer graphene is first transferred out from a substrate by pure Au pads and then transferred with Au pads onto monolayer MoS<sub>2</sub> as electrodes. In this way, the monolayer graphene, as a buffer layer of electrodes, remains intact and defect-free (Figure 1c), which surpasses defective graphene buffer layers induced by metal deposition reported in literature.<sup>[22-24]</sup> Benefitting from the atomically flat surface and adjustable Fermi level of monolayer graphene, the MoS<sub>2</sub> devices with t-Au/graphene electrodes have reduced Schottky barrier heights (SBHs) of 47 meV and small contact resistances of 4.7 k $\Omega$ · $\mu$ m at a carrier density of 3.2 $\times$ 10<sup>12</sup> cm<sup>-2</sup>. These lead to a much larger on-state current ( $I_{on}$ ) and higher carrier mobility compared to the devices with deposited metal electrodes or only with transferred Au electrodes. More importantly, the defect-free, hydrophobic graphene buffer layer prevents metal diffusion from electrodes to MoS<sub>2</sub> and the intercalation of water molecules at the electrode-MoS<sub>2</sub> interfaces, enabling high resistances of MoS<sub>2</sub> devices to harsh environments, including humid, oxidizing, and high-temperature environments.

This article is protected by copyright. All rights reserved.

Under 100% relative humidity, the t-Au/graphene-MoS<sub>2</sub> transistor changes much less (~6%) in on-state current than the devices with deposited Ti/Au or with transferred Au electrodes. It also exhibits much more stable electrical transport properties in oxidizing environments (air) or even after annealing at 350 °C compared to devices with conventional Ti/Au electrodes or with emerging Bi/Au electrodes. These advantages have the MoS<sub>2</sub> devices with t-Au/graphene electrodes possess the optimal performance among all kinds of electrode designs if comprehensively considering the mobility, on-state current, humid-resistance, oxygen-resistance, and thermal stability (Figure 1d).

## 2. Results and discussion

The all-transfer process of t-Au/graphene electrodes for fabricating MoS<sub>2</sub> field-effect transistors (FETs) is schematically illustrated in **Figure 2a**. In general, the all-transfer process includes the transfer of monolayer graphene onto a transition substrate, the transfer of Au pads onto the monolayer graphene, and the transfer of Au/graphene pads onto MoS<sub>2</sub> as electrodes. In all of these steps, the electrode-channel interfaces keep clean and defect-free, which is critical for harsh-environment-resistant devices. First, high-quality monolayer graphene synthesized by CVD as reported was transferred from the growth substrate (copper foil) onto a clean transition SiO<sub>2</sub>/Si substrate.<sup>[25,26]</sup> Then, prepatterned Au pads made by photolithography and e-beam evaporating deposition were transferred onto monolayer graphene through the electrode transfer technique, and O<sub>2</sub> plasma was used to remove the exposed graphene region uncovered by Au pads (Step 1 in Figure 2a). After that, polymethyl methacrylate (PMMA) was spin-coated onto the sample, and the graphene/Au/PMMA layer was detached from the transition substrate by a polydimethylsiloxane (PDMS) film with the assistance of water wedging (Step 2 in Figure 2a)<sup>[27,28]</sup>. Finally, the Au/graphene electrodes were aligned with monolayer MoS<sub>2</sub> on a target SiO<sub>2</sub>/Si substrate to fabricate vdW-contacted devices (Step 3 in Figure 2a). Figure 2b shows optical images of the large-area monolayer graphene grown on a copper foil (topleft panel), transferred onto the transition SiO<sub>2</sub>/Si substrate (bottomleft panel), and detached by Au/PDMS (topright panel). After detached from the transition substrate by Au/PDMS, monolayer graphene is uniformly attached to the Au pads, as confirmed by the uniform mapping intensity of Raman signals (Figure 2b, bottomright panel). The ratio of the 2D (1594 cm<sup>-1</sup>) to G (2697 cm<sup>-1</sup>) peak intensity of graphene is larger than 2, which confirms the features of monolayers (Figure

This article is protected by copyright. All rights reserved.

2c). The monolayer graphene keeps having negligible D peaks at  $\sim 1350 \text{ cm}^{-1}$  after transferred onto the transition  $\text{SiO}_2/\text{Si}$  substrate and further detached from the transition substrate (i.e., transferred on Au), suggesting that it remains intact and defect-free throughout the entire all-transfer process (Figure 2c). In contrast, direct deposition of Au on monolayer graphene to prepare Au/graphene electrodes, following the method reported in literature,<sup>[22,23]</sup> leads to much defective graphene, as revealed by an apparent D peak in the Raman spectrum (Figure 2c), which is not favourable for devices working in harsh environments. These results suggest that our all-transfer method can retain the integrity and high quality of monolayer graphene to the maximum extent, which is critical to harsh-environment-resistant  $\text{MoS}_2$  devices.

The  $\text{MoS}_2$  monolayers used for the devices were also synthesized by CVD (see details in Methods). Atomic force microscopy (AFM) images and Raman spectra in Figure S1 show that the as-grown  $\text{MoS}_2$  has a thickness of 0.7 nm with an atomically flat surface, and the interval between the in-plane  $E_{2g}^1$  vibrational Raman mode and the out-of-plane  $A_{1g}$  Raman mode is  $\sim 21 \text{ cm}^{-1}$ , both revealing the monolayer characteristic of  $\text{MoS}_2$ .<sup>[29]</sup> In addition to  $\text{MoS}_2$  devices with t-Au/graphene electrodes, we also fabricated devices with other kinds of electrodes, i.e., transferred Au (t-Au), e-beam deposited Ti/Au (d-Ti/Au), and e-beam deposited Bi/Au (d-Bi/Au) (see Methods for details). All of the transfer curves of  $\text{MoS}_2$  FETs with different kinds of electrodes exhibit typical n-type transport properties, while the  $\text{MoS}_2$  FETs with t-Au/graphene show the highest source-drain current ( $I_{ds}$ ) (Figure 2d) and a high on/off current ratio of  $10^7$  (Figure 1d). The linear and symmetric output curves, as shown in Figure 1e, also indicate good ohmic contacts between the  $\text{MoS}_2$  channel and the t-Au/graphene electrodes.

The field-effect mobility  $\mu_{EF}$  is estimated by the following equation:

$$\mu_{EF} = \frac{dI_{ds}}{dV_{gs}} \cdot \frac{L}{V_{ds}WC_{ox}} \quad (1)$$

where L and W are the channel length and width, respectively, and  $C_{ox}$  is the capacitance per unit area of  $\text{SiO}_2$ . As shown in Figure 2e, the  $\text{MoS}_2$  transistors with t-Au/graphene electrodes exhibit the highest mobility of  $34 \pm 5 \text{ cm}^2 \text{ V}^{-1} \text{ s}^{-1}$  and the highest on-state current of  $10 \pm 1 \mu\text{A}/\mu\text{m}$  among all four kinds of electrodes. The improvement in the mobility and on-state current for the t-Au/graphene electrodes can be attributed to the following two aspects. On the one hand, atomically flat graphene and  $\text{MoS}_2$  form good vdW contacts, alleviating the FLP effect between  $\text{MoS}_2$  and Au electrodes. On

This article is protected by copyright. All rights reserved.

the other hand, the Fermi level of graphene can be regulated by gate voltage to better match the energy band of MoS<sub>2</sub>, resulting in a lower barrier height (Figure 1c). To estimate the barrier height between MoS<sub>2</sub> and the electrodes, we measured the transfer curves of MoS<sub>2</sub> devices at different temperatures (Figure S2). According to the thermionic emission model,<sup>[30]</sup> the effective contact barrier height  $\Phi_b$  can be estimated from the slope of the  $\ln(I_{ds}/T^{3/2})$  versus  $1/T$  relationship at various  $V_{gs}$  values (Figure 2f). As shown in Figure 2f, SBH is extracted from the flat-band condition, which corresponds to the onset of deviations from the linear region. The SBH between MoS<sub>2</sub> and t-Au/graphene is thus estimated to be 47 meV, which is much lower than that for the t-Au electrodes (100 meV) and d-Bi/Au electrodes (82 meV) (Figure S2). This reduction in the SBH caused by the assistance of graphene is also supported by the low contact potential difference between graphene and MoS<sub>2</sub> (17.2 mV), which is much lower than that between Au and MoS<sub>2</sub> (84.7 mV), as measured by Kelvin force probe microscopy (KPFM) (Figure S3).

To verify the better electrical contact between MoS<sub>2</sub> and t-Au/graphene electrodes, transmission line method (TLM) measurement is used to extract the contact resistance ( $R_c$ ) of MoS<sub>2</sub> transistors where rectangular monolayer MoS<sub>2</sub> was defined by direct laser patterning (Figure S4a).<sup>[31]</sup> The transport properties of MoS<sub>2</sub> FETs with different channel lengths and carrier densities are measured, and the carrier density is estimated by

$$n = \frac{C_{ox}}{q} \cdot (V_{gs} - V_{th}) \quad (2)$$

where  $C_{ox}$  is the capacitance per unit area of 300-nm-thick SiO<sub>2</sub> and  $V_{th}$  is the threshold voltage obtained by the linear extrapolation method for each channel (Figure S4c). Figure 2g shows the good linear fitting of the dependence of the total resistance on the channel length at different carrier densities, suggesting the uniformity of the channel material and the consistency of electrode contacts for the MoS<sub>2</sub> transistor with t-Au/graphene electrodes. The ordinate intercept of these lines corresponds to twice the width-normalized contact resistance  $R_c$ . As shown in Figure S4e,  $R_c$  decreases with increasing carrier density  $n$  of MoS<sub>2</sub>, and it is apparently lower for the t-Au/graphene electrodes than for the t-Au electrodes at any value of  $n$ . At  $V_{gs} = 60$  V, the  $R_c$  of the t-Au-MoS<sub>2</sub> contact is 18.5 k $\Omega$ · $\mu$ m, while it is only 4.7 k $\Omega$ · $\mu$ m for the t-Au/graphene-MoS<sub>2</sub> contact. The lower contact resistance results from the reduced SBH because the contact resistance is exponentially proportional to SBH.<sup>[32]</sup> The benchmark plot shows that the contact resistance of the t-Au/graphene-MoS<sub>2</sub>

This article is protected by copyright. All rights reserved.

transistors in this work is apparently lower than those made by other graphene buffer layer methods<sup>[22, 23, 33]</sup>, in which defective graphene may be used due to metal deposition (Figure S4f). The mobility, on-state current, Schottky barrier height, and contact resistance of the t-Au/graphene-contacted MoS<sub>2</sub> device have been comparable to the reported values of FETs based on atmospheric-pressure CVD monolayer MoS<sub>2</sub>,<sup>[9,34]</sup> and can be further optimized by improving the sample quality, employing high-k dielectric materials, and shortening the channel length.<sup>[15, 35]</sup>

Harsh environments are critical factors that may influence and even severely decay the performance of nanoscale electronic devices. Even for well packaged devices, water and oxygen molecules may permeate through defects or cracks of the packaging materials (such as epoxy molding compounds) and degrade the devices by interface chemical or electrochemical reactions.<sup>[36-39]</sup> Moreover, appropriate packaging of 2D devices still remains a great challenge.<sup>[40,41]</sup> Therefore, improvement of intrinsic harsh-environment resistances is of vital importance for long-lifetime 2D TMDC devices.

Humid environment is one of the most common harsh environments where devices work. We tested the performance of MoS<sub>2</sub> devices with different electrodes in a humid environment. **Figure 3a** shows the transfer curves of the t-Au/graphene-contacted MoS<sub>2</sub> transistor at  $V_{ds} = 0.5$  V under different relative humidity (RH) that is controlled by homemade equipment (Figure S5a). With the increase in RH, the t-Au/graphene-contacted MoS<sub>2</sub> device shows only very little change in the on-state current at high gate voltages and in the threshold voltage ( $V_{th}$ ) (Figure 3a and inset), while the devices with other electrodes exhibit much larger changes in transfer curves (Figure S5). As shown in Figure 3b, the on-state current of the device with t-Au/graphene contacts at  $V_{gs} = 40$  V changes by less than 6% when RH varies from 0 to 100%. In contrast, the on-state currents for the t-Au-contacted and d-Ti/Au-contacted devices change by ~21% and ~23%, respectively, showing much larger instability to the humid environment. Moreover, the threshold voltage shift ( $\Delta V_{th}$ ) of the t-Au/graphene-contacted MoS<sub>2</sub> device is less than 1 V under 100% RH, which is much smaller than the devices with other electrodes (Figure 3c). The high resistance of the t-Au/graphene-contacted device to a humid environment should result from the perfect vdW interface contacts between graphene and MoS<sub>2</sub> as well as the hydrophobicity of graphene (contact angle of  $92 \pm 1^\circ$ , Figure 3d), which effectively prevents H<sub>2</sub>O molecules from intercalating into the electrode-MoS<sub>2</sub> interfaces. For t-Au contacts, the hydrophilicity of Au ( $72 \pm 3^\circ$ , Figure 3d) would have H<sub>2</sub>O molecules enter the interface more easily,

This article is protected by copyright. All rights reserved.

thus degrading the MoS<sub>2</sub> FETs due to carrier scattering and *p*-doping in MoS<sub>2</sub>. In addition, the increased current of the MoS<sub>2</sub> device with d-Ti/Au electrodes at high RH may result from the TiO<sub>x</sub> formed at the electrode-channel interface (Figure S6).

To further understand the mechanism for the enhancement of humidity resistance of the t-Au/graphene-contacted MoS<sub>2</sub> devices, we performed density functional theory (DFT) calculations to investigate the t-Au/MoS<sub>2</sub> and t-Au/graphene/MoS<sub>2</sub> interfaces (Figure 3e, see Methods for details). The formation energy ( $E_f$ ) of adsorption of an H<sub>2</sub>O molecule in a series of Au/graphene/MoS<sub>2</sub> and Au/MoS<sub>2</sub> configurations with different contact distances was calculated (Figure S7 and inset of Figure 3e). Figure 3e shows that the formation energy of an H<sub>2</sub>O molecule first decreases with the contact distance increasing up to 0.6 nm, and then slightly increases when the contact distance further enlarges from 0.6 to 0.7 nm (see Figure S8 and more discussions in Supporting Information). At a contact distance of 0.5 nm, which is the common vdW gap between the transferred electrode and 2D TMDCs,<sup>[42,43]</sup> the formation energy of an H<sub>2</sub>O molecule in Au/graphene/MoS<sub>2</sub> and Au/MoS<sub>2</sub> configurations is 0.03 eV and -0.34 eV, respectively. This result indicates that the diffusion of H<sub>2</sub>O molecules into the interface of t-Au and MoS<sub>2</sub> is spontaneous, but the graphene buffer layer can effectively avoid the intercalation of H<sub>2</sub>O molecules, leading to a much more stable performance of the t-Au/graphene-contacted device in a highly humid environment.

In addition to high humidity, the oxidizing environment is also harsh for electronic devices. For example, oxygen can adsorb on channel or electrode materials, diffuse into their interfaces, or further oxidize them even under a low local oxygen pressure in the case of packaging, which is usually the reason for the degradation of many devices. It is reported that the MoS<sub>2</sub> channel would be *p*-doped by physically adsorbed O<sub>2</sub> and H<sub>2</sub>O molecules, but these adsorbed molecules can be removed by annealing in vacuum or in inert atmospheres.<sup>[44]</sup> Consequently, for the device where only the channel region is exposed and other regions are covered by PMMA, the drain-source current ( $I_{ds}$ ) in the transfer curve decreases after a 12 h treatment in an oxygen-containing and humid environment but returns to its pristine value after annealing at 200 °C (Figure S9), which means that the resulting change in transport properties due to the adsorption of O<sub>2</sub> and H<sub>2</sub>O on the MoS<sub>2</sub> channel region is reversible. However, the diffusion of oxygen molecules into electrode-MoS<sub>2</sub> interfaces and the induced oxidization of electrodes may permanently change the structure of electrodes, leading to unrecoverable device performance.<sup>[20]</sup>

This article is protected by copyright. All rights reserved.

To investigate the stability of electrical contacts in an oxidizing environment, we placed MoS<sub>2</sub> devices with different electrodes under an environmental pressure of 10 mbar (80% N<sub>2</sub> and 20% O<sub>2</sub> in volume ratio) for a long time. Note that before electrical measurements, all the devices were annealed in Ar at 200 °C to remove possible adsorbed molecules on the MoS<sub>2</sub> channel, and the transfer curves are shown in Figure S10. After 6 months, the resistance of the t-Au/graphene-contacted device at  $V_{gs} = 40$  V remains nearly unchanged (increases by <15%), while those of the d-Bi/Au-MoS<sub>2</sub> device and d-Ti/Au-MoS<sub>2</sub> devices increase by ~780% and ~410%, respectively (**Figure 4a**). Moreover, the t-Au/graphene-contacted device shows no apparent shift of threshold voltages after 6 months, while the d-Bi/Au and d-Ti/Au devices exhibit large positive threshold voltage shifts of 7 V and 22 V, respectively (Figure S10d). In addition to a low oxygen pressure environment, the t-Au/graphene-contacted device also exhibits a negligible on-state current change ( $|\Delta I_{on}/I_{on}|$ ) of only 4% after being exposed to a pure O<sub>2</sub> environment for 10 h followed by annealing at 200 °C in pure Ar to remove the adsorbed molecules on the MoS<sub>2</sub> channel (Figure S11).

These results suggest that the t-Au/graphene-contacted MoS<sub>2</sub> device is much more stable than the devices with deposited electrodes in oxidizing environments. Such high oxygen resistance of the t-Au/graphene-contacted MoS<sub>2</sub> device should be attributed to the good stability of each electrode component, especially to the perfect chemical and structural stability of the defect-free graphene buffer layer. In contrast, Bi and Ti buffer layers for electrodes are prone to oxidation, resulting in apparent resistance increases of the d-Bi/Au- and d-Ti/Au-contacted MoS<sub>2</sub> devices. Figure 4b and 4c show X-ray photoemission spectra (XPS) of the d-Bi/Au and d-Ti/Au electrodes used in the MoS<sub>2</sub> devices, respectively. Note that to collect the signals of Bi and Ti, Ar ions were used to remove the top-layer Au. For as-prepared d-Bi/Au, Bi 4f<sub>7/2</sub> (156.9 eV) and 4f<sub>5/2</sub> (162.2 eV) peaks arise from metallic Bi<sup>0</sup>, and Bi 4f<sub>7/2</sub> (158.4 eV) and 4f<sub>5/2</sub> (164.0 eV) peaks arise from Bi<sup>3+</sup>.<sup>[45]</sup> After exposure to air for two weeks, the peak area ratio of Bi<sup>3+</sup>/Bi<sup>0</sup> increases from 0.32 to 0.81, verifying the oxidation of the d-Bi/Au electrodes. For as-prepared d-Ti/Au, Ti 2p<sub>3/2</sub> (454.3 eV) and 2p<sub>1/2</sub> (460.4 eV) peaks arise from metallic Ti<sup>0</sup>,<sup>[46]</sup> and peaks at 456.2 eV and 462.2 eV arise from Ti<sup>3+</sup>, which may originate from the substoichiometric oxides of Ti during the evaporation process.<sup>[47]</sup> After exposure to air for two weeks, the Ti<sup>0</sup> peaks disappear, while the emerging Ti 2p<sub>3/2</sub> peaks at 456.3 eV and 458.9 eV correspond to Ti<sup>3+</sup> and Ti<sup>4+</sup>, respectively,<sup>[48]</sup> also confirming the oxidation of the d-Ti/Au electrodes.

This article is protected by copyright. All rights reserved.

High temperature is another kind of harsh environment to disable devices by failing their working mechanism or destroying materials. Because of the increasing heat generation in the case of high device integration, devices that can withstand temperatures higher than 125 °C are much desired in modern electronics. Although the MoS<sub>2</sub> channel is quite stable at temperatures up to 350 °C in a low-pressure environment,<sup>[49]</sup> metal electrodes with low work-function buffer layers such as Ti and Bi are not suitable for high-temperature applications because they suffer from gradual oxidization even at a low partial pressure of oxygen. In addition to oxidization, diffusion of electrode metals into the MoS<sub>2</sub> channel and possible chemical reaction between them at high temperature may also degrade the device. Figure 4d shows that both the d-Au/Ti-contacted and d-Au/Bi-contacted MoS<sub>2</sub> devices degrade after annealing at 350 °C for 1 h, even under the protection of high-purity Ar (99.999%). In particular, the  $I_{ds}$  of the d-Bi/Au-contacted MoS<sub>2</sub> device declines significantly by more than 70%. In contrast, the t-Au/graphene-MoS<sub>2</sub> device remains intact under the same high-temperature conditions, as revealed by the unchanged transfer curve (Figure 4d) as well as the identical optical and AFM images (Figure S13). This high-temperature resistance of the t-Au/graphene-contacted MoS<sub>2</sub> device should benefit from the inert graphene buffer layer, which avoids the oxidization of electrodes and prevents the diffusion of metals into the channel.<sup>[50]</sup>

The higher resistance of the t-Au/graphene-MoS<sub>2</sub> device to high temperature can be further revealed by Raman spectroscopy. As shown in Figure S14, there is no distinct D peak at ~1350 cm<sup>-1</sup> after graphene is annealed at 300 °C in air, suggesting that no defects are introduced into graphene at this temperature. The t-Au/graphene-contacted MoS<sub>2</sub> also does not show apparent structural changes after annealing at 350 °C for 1 h in Ar, as revealed by the unchanged Raman peak positions and intensities of both the in-plane vibration mode,  $E_{2g}^1$ , and the out-of-plane vibrational mode,  $A_{1g}$  (Figure 4e). Note that the Raman signal is obtained from the back side of transparent sapphire (Figure S15). However, both the  $E_{2g}^1$  and  $A_{1g}$  modes of the d-Ti/Au-contacted MoS<sub>2</sub> weaken after the same annealing (Figure 4e), which implies partial damage to MoS<sub>2</sub> at the electrode-channel interfaces due to oxidization or reaction. For the d-Bi/Au-contacted device, such damage may be more severe due to the low melting point of Bi metal (271 °C), which is also revealed by the dark-colour pinholes appearing on the electrode surface (Figure S16). Owing to the robust interface structure of the t-Au/graphene electrodes, the SBH of the t-Au/graphene contact changes very slightly (from 80 to 63 meV) after a sequence of annealing at 350°C for 1.5 h (Figure 4f, also see Figure S17 for detailed calculation of SBH).

This article is protected by copyright. All rights reserved.

However, both SBHs apparently increase for the d-Bi/Au contact (from 110 to 140 meV) and the d-Ti/Au contact (from 175 meV to 215 meV), which further verifies the damage of the electrode interfaces due to oxidization of MoS<sub>2</sub> or metal diffusion at high temperatures.

Furthermore, we conducted cyclic tests on the t-Au/graphene-contacted MoS<sub>2</sub> device in a typical humid environment (RH=50%, Figure S18a-c) and at a typical high temperature (T=150 °C, Figure S18d-f), respectively. As shown in Figure S18a and d, the transfer characteristics of the device are nearly unchanged after 1000 cycles whether in the humid environment or at the high temperature. The on-state current ( $I_{on}$ ), threshold voltage ( $V_{th}$ ), and hysteresis of the device extracted from the cyclic transfer curves also remain almost unchanged (Figure S18b, c, e, and f). For example, after 1000 cyclic tests in the humid environment,  $I_{on}$  only changes by 3% and the threshold voltage by less than 0.6 V (Figure S18b), while the small hysteresis of the device (about 1.0-2.5 V) remains almost unchanged (Figure S18c). In addition, we also performed a cyclic pulse test for the t-Au/graphene-contacted MoS<sub>2</sub> device at RH= 50%. In this cyclic pulse test,  $V_{gs}$  pulses of various time periods ( $V_{gs}$ =40V, for 0.1 s, 0.2 s and 0.5 s) are applied on the device for cycles and  $I_{ds}$  is recorded at  $V_{gs}$ =40V and 0V during the cyclic pulses. As shown in Figure S19, the  $I_{ds}$  values only show very slight decreases by only 4% at  $V_{gs}$ =40V and by 8% at  $V_{gs}$ =0V after 1440 pulses. All of the above cyclic tests verify the very good reliability of the t-Au/graphene-contacted MoS<sub>2</sub> device in harsh environments.

We finally tested the device performance in a complicated harsh environment that involves humidity, oxygen, and high temperatures by placing MoS<sub>2</sub> devices with different kinds of electrodes in a homemade chamber under an atmosphere containing 80% wet Ar (saturated) and 20% dry O<sub>2</sub> for 12 h and then annealed at 200 °C in Ar (Figure S20a). As shown in Figure S20f, the t-Au/graphene-contacted MoS<sub>2</sub> device exhibits negligible resistance changes after treatment and annealing, while the resistance of the d-Ti/Au-MoS<sub>2</sub> and d-Bi/Au-MoS<sub>2</sub> devices increases by more than 50%. Therefore, the t-Au/graphene-MoS<sub>2</sub> device further shows great potential for working in complicated harsh environments.

### 3. Conclusion

This article is protected by copyright. All rights reserved.

In conclusion, we demonstrate harsh-environment-resistant MoS<sub>2</sub> devices through an all-transfer method of t-Au/graphene electrodes. With intact and defect-free monolayer graphene as the buffer layer of electrodes, the MoS<sub>2</sub> devices show a reduced SBH of 47 meV and low contact resistance of 4.7 kΩ·μm. These properties lead to a much larger on-state current ( $I_{on}$ ) and higher carrier mobility compared to devices with deposited metal electrodes or only with transferred Au electrodes. Both experimental measurements and DFT calculations show that the hydrophobicity of defect-free monolayer graphene effectively avoids the intercalation of H<sub>2</sub>O molecules. As a result, the t-Au/graphene-MoS<sub>2</sub> device exhibits little change in the on-state current (~6%) even under 100% relative humidity. Furthermore, the t-Au/graphene-MoS<sub>2</sub> devices also show much better stability in oxygen-containing environments or after experiencing high temperatures compared to d-Ti/Au- or d-Bi/Au-contacted devices. These advantages have the t-Au/graphene-contacted MoS<sub>2</sub> devices possess optimal performance after comprehensively considering the mobility, on-state current, humid-resistance, oxygen-resistance, and thermal stability (Figure 1d). Our work provides a promising interface engineering strategy for the application of 2D devices in harsh environments.

#### 4. Methods

*Synthesis and transfer of MoS<sub>2</sub> and graphene:* Monolayer MoS<sub>2</sub> was synthesized by CVD on a 300 nm SiO<sub>2</sub>/Si substrate using 5 mg MoO<sub>3</sub> (99.95%, Aladdin) and 10 mg sulphur (99.99%, Aladdin) powders as precursors and with the help of perylene-3,4,9,10 tetracarboxylic acid tetrapotassium salt (PTAS). A piece of SiO<sub>2</sub>/Si substrate was faced down and placed on the MoO<sub>3</sub> powder. Before heating, the whole CVD system was purged with 200 standard cubic centimetres per minute (sccm) Ar gas for 10 min. Then, the temperature of MoO<sub>3</sub> was ramped to 650 °C at a rate of 15 °C/min and stayed at 650 °C for 3 min with 5 sccm Ar. The temperature of sulfur powder heated by a heating belt ramped to 180 °C at a rate of 30 °C/min as soon as the temperature of MoO<sub>3</sub> reached 500 °C. After growth, the furnace was opened for rapid cooling. Polymethyl methacrylate (PMMA) coating and KOH etching were used to transfer the synthesized monolayer MoS<sub>2</sub> to a new substrate. Monolayer graphene was synthesized by the CVD method. First, a polycrystalline Cu foil (25 μm thick, 99.8%, Sichuan Oriental Stars Trading Co. Ltd, #Cu-1031) was placed on a quartz substrate and loaded into the CVD furnace (Tianjin Kaiheng Co. Ltd). Then, the system was heated to 1020 °C for 1 hour under 500 sccm Ar and 10

This article is protected by copyright. All rights reserved.

sccm H<sub>2</sub> to obtain single-crystal Cu (111). After that, 0.01 sccm CH<sub>4</sub> was introduced into the system for 30 minutes to obtain monolayer graphene. Finally, the system was naturally cooled under the same reducing atmosphere. The growth was carried out under atmospheric pressure. To transfer the graphene film onto SiO<sub>2</sub>/Si substrates, the as-grown graphene film on Cu foil was spin-coated with PMMA at 2000 rpm for 1 min, and the back side was cleaned by O<sub>2</sub> plasma. The Cu substrate was etched away by (NH<sub>4</sub>)<sub>2</sub>S<sub>2</sub>O<sub>8</sub> solution (0.01 g·mL<sup>-1</sup>) over 6 h. The film was washed with deionized water, placed on SiO<sub>2</sub>/Si substrates, and dried at 120 °C. Finally, the PMMA was removed by acetone.

*Device fabrication:* T-Au/graphene electrodes were obtained by a self-aligned and lithography-free transfer method. Then, Au/graphene electrodes were transferred onto MoS<sub>2</sub> through a homemade deterministic transfer stage under an optical microscope. Finally, acetone soaking was used to remove the PMMA, and a monolayer MoS<sub>2</sub> FET with Au/graphene electrodes was fabricated. MoS<sub>2</sub> devices with Ti or Bi contact were fabricated by standard electron-beam lithography and electron-beam deposition (1 × 10<sup>-6</sup> mbar) with 10 nm Ti (0.5 Å/s) or Bi (0.5 Å/s) and 50 nm Au (1 Å/s).

*Characterizations:* Optical microscope (Olympus, BX51M) and atomic force microscope (Bruker Multimode 8) were used to characterize the surface morphology of MoS<sub>2</sub> and graphene. SmartRaman confocal-micro-Raman module (Institute of Semiconductors, Chinese Academy of Sciences) was used for Raman measurement with a ×100 objective lens (NA = 0.90) under the backscattering geometry, which is coupled with a Horiba iHR550 spectrometer and a charge-coupled device (CCD) detector. X-ray photoelectron spectroscopy experiments were conducted on a Thermo Fisher ESCALAB Xi. The electrical measurements of devices were carried out with an Agilent B1500A semiconductor parameter analyser.

*DFT calculations:* The DFT calculations were performed by using the Vienna Ab initio Simulation Package (VASP) program.<sup>[51,52]</sup> The generalized gradient approximation with the Perdew-Burke-Ernzerhof type exchange-correlation functional (GGA-PBE) and projector augmented wave (PAW) method were adopted in all the calculations.<sup>[53,54]</sup> The plane-wave energy cutoff was fixed at 530 eV, and a 3 × 3 × 1 Monkhorst-Pack grid was used for the k-point sampling. The vdW interactions were involved by using the DFT-D3 method of Grimme.<sup>[55]</sup> A smearing of 0.1 eV is used. The convergence of energy and maximum force were set to 10<sup>-5</sup> eV and 5 × 10<sup>-3</sup> eV/Å, respectively. For the calculations of the adsorption energies of H<sub>2</sub>O molecules inserted into the interface of MoS<sub>2</sub>/Au and

MoS<sub>2</sub>/graphene/Au, a (3×3) supercell of Au (111) with four atomic layers was built. An additional (2√3 × 2√3) R30° unit cell of graphene was adsorbed on the Au (111) surface for the MoS<sub>2</sub>/Gr/Au model. Then, a (√7 × √7) R11° unit cell of MoS<sub>2</sub> was adsorbed on the Au (111) surface or graphene, with the contact distances set to 4, 5, 6 and 7 Å. A H<sub>2</sub>O molecule was adsorbed under the MoS<sub>2</sub> layer. The adsorption energy of the H<sub>2</sub>O molecule is defined as

$$E_{f1} = E_{\text{MoS}_2/\text{H}_2\text{O}/\text{Au}} - E_{\text{MoS}_2/\text{Au}} - E_{\text{H}_2\text{O}} \quad (3)$$

$$E_{f2} = E_{\text{MoS}_2/\text{H}_2\text{O}/\text{Gr}/\text{Au}} - E_{\text{MoS}_2/\text{Gr}/\text{Au}} - E_{\text{H}_2\text{O}} \quad (4)$$

where  $E_{\text{MoS}_2/\text{H}_2\text{O}/\text{Au}}$ ,  $E_{\text{MoS}_2/\text{Au}}$ ,  $E_{\text{MoS}_2/\text{H}_2\text{O}/\text{Gr}/\text{Au}}$  and  $E_{\text{MoS}_2/\text{Gr}/\text{Au}}$  are the energies of the MoS<sub>2</sub>/Au model with and without the H<sub>2</sub>O molecule and the energies of the MoS<sub>2</sub>/Gr/Au model with and without the H<sub>2</sub>O molecule, respectively.  $E_{\text{H}_2\text{O}}$  is the energy of the H<sub>2</sub>O molecule in vacuum.

### Supporting Information

Supporting Information is available from the Wiley Online Library or from the author.

### Acknowledgements

Y.W. and Z.X. contributed equally to this work. This work was financially supported by National Key R&D Program of China (2018YFA0208401), Basic Science Center Project of NSFC under grant No. 51788104, National Natural Science Foundation of China (51972193, 520250023), and Guangdong Major Project of Basic and Applied Basic Research (2021B0301030002).

Received: ((will be filled in by the editorial staff))

Revised: ((will be filled in by the editorial staff))

Published online: ((will be filled in by the editorial staff))

This article is protected by copyright. All rights reserved.

## References

- [1] M. M. Waldrop, *Nature* **2016**, 530, 144.
- [2] C. Auth, A. Aliyarukunju, M. Asoro, D. Bergstrom, V. Bhagwat, J. Birdsall, N. Bisnik, M. Buehler, V. Chikarmane, G. Ding, presented at *2017 IEEE International Electron Devices Meeting (IEDM)*, **2017**.
- [3] 2020 International Roadmap for Devices and Systems (IRDS™), <https://irds.ieee.org/> (accessed 2022-11-07).
- [4] M. Chhowalla, D. Jena, H. Zhang, *Nat. Rev. Mater.* **2016**, 1, 1.
- [5] C. Liu, H. Chen, S. Wang, Q. Liu, Y. G. Jiang, D. W. Zhang, M. Liu, P. Zhou, *Nat. Nanotechnol.* **2020**, 15, 545.
- [6] D. Akinwande, C. Huyghebaert, C. H. Wang, M. I. Serna, S. Goossens, L. J. Li, H. P. Wong, F. H. L. Koppens, *Nature* **2019**, 573, 507.
- [7] S. Song, Y. Sim, S.-Y. Kim, J. H. Kim, I. Oh, W. Na, D. H. Lee, J. Wang, S. Yan, Y. Liu, J. Kwak, J.-H. Chen, H. Cheong, J.-W. Yoo, Z. Lee, S.-Y. Kwon, *Nat. Electron.* **2020**, 3, 207.
- [8] C. Kim, I. Moon, D. Lee, M. S. Choi, F. Ahmed, S. Nam, Y. Cho, H. J. Shin, S. Park, W. J. Yoo, *ACS Nano* **2017**, 11, 1588.
- [9] P. C. Shen, C. Su, Y. Lin, A. S. Chou, C. C. Cheng, J. H. Park, M. H. Chiu, A. Y. Lu, H. L. Tang, M. M. Tavakoli, G. Pitner, X. Ji, Z. Cai, N. Mao, J. Wang, V. Tung, J. Li, J. Bokor, A. Zettl, C. I. Wu, T. Palacios, L. J. Li, J. Kong, *Nature* **2021**, 593, 211.
- [10] S. Das, H. Y. Chen, A. V. Penumatcha, J. Appenzeller, *Nano Lett.* **2013**, 13, 100.
- [11] J. Wang, Q. Yao, C. W. Huang, X. Zou, L. Liao, S. Chen, Z. Fan, K. Zhang, W. Wu, X. Xiao, C. Jiang, W. W. Wu, *Adv. Mater.* **2016**, 28, 8302.
- [12] A. Dankert, L. Langouche, M. V. Kamalakar, S. P. Dash, *ACS Nano* **2014**, 8, 476.
- [13] J. Jang, Y. Kim, S. S. Chee, H. Kim, D. Whang, G. H. Kim, S. J. Yun, *ACS Appl. Mater. Interfaces* **2020**,

This article is protected by copyright. All rights reserved.

- 12, 5031.
- [14] K. Andrews, A. Bowman, U. Rijal, P. Y. Chen, Z. X. Zhou, *ACS Nano* **2020**, *14*, 6232.
- [15] Y. Liu, J. Guo, E. Zhu, L. Liao, S. J. Lee, M. Ding, I. Shakir, V. Gambin, Y. Huang, X. Duan, *Nature* **2018**, *557*, 696.
- [16] Y. Jung, M. S. Choi, A. Nipane, A. Borah, B. Kim, A. Zangiabadi, T. Taniguchi, K. Watanabe, W. J. Yoo, J. Hone, J. T. Teherani, *Nat. Electron.* **2019**, *2*, 187.
- [17] D. Akinwande, N. Petrone, J. Hone, *Nat. Commun.* **2014**, *5*, 5678.
- [18] J. Watson, G. Castro, *J. Mater. Sci.: Mater. Electron.* **2015**, *26*, 9226.
- [19] M. Lanza, Q. Smets, C. Huyghebaert, L. J. Li, *Nat. Commun.* **2020**, *11*, 5689.
- [20] S. McDonnell, C. Smyth, C. L. Hinkle, R. M. Wallace, *ACS Appl. Mater. Interfaces* **2016**, *8*, 8289.
- [21] K. M. Freedy, H. Zhang, P. M. Litwin, L. A. Bendersky, A. V. Davydov, S. McDonnell, *ACS Appl. Mater. Interfaces* **2019**, *11*, 35389.
- [22] S. S. Chee, D. Seo, H. Kim, H. Jang, S. Lee, S. P. Moon, K. H. Lee, S. W. Kim, H. Choi, M. H. Ham, *Adv. Mater.* **2019**, *31*, e1804422.
- [23] L. Yu, Y. H. Lee, X. Ling, E. J. Santos, Y. C. Shin, Y. Lin, M. Dubey, E. Kaxiras, J. Kong, H. Wang, T. Palacios, *Nano Lett.* **2014**, *14*, 3055.
- [24] D. Yuchen, Y. Lingming, Z. Jingyun, L. Han, K. Majumdar, P. D. Kirsch, P. D. Ye, *IEEE Electron Device Lett.* **2014**, *35*, 599.
- [25] M. Wu, Z. Zhang, X. Xu, Z. Zhang, Y. Duan, J. Dong, R. Qiao, S. You, L. Wang, J. Qi, D. Zou, N. Shang, Y. Yang, H. Li, L. Zhu, J. Sun, H. Yu, P. Gao, X. Bai, Y. Jiang, Z. J. Wang, F. Ding, D. Yu, E. Wang, K. Liu, *Nature* **2020**, *581*, 406.
- [26] X. Z. Xu, Z. H. Zhang, J. C. Dong, D. Yi, J. J. Niu, M. H. Wu, L. Lin, R. K. Yin, M. Q. Li, J. Y. Zhou, S. X. Wang, J. L. Sun, X. J. Duan, P. Gao, Y. Jiang, X. S. Wu, H. L. Peng, R. S. Ruoff, Z. F. Liu, D. P. Yu, E. G. Wang, F. Ding, K. H. Liu, *Sci. Bull.* **2017**, *62*, 1074.

This article is protected by copyright. All rights reserved.

- [27] Y. Huang, Y. H. Pan, R. Yang, L. H. Bao, L. Meng, H. L. Luo, Y. Q. Cai, G. D. Liu, W. J. Zhao, Z. Zhou, L. M. Wu, Z. L. Zhu, M. Huang, L. W. Liu, L. Liu, P. Cheng, K. H. Wu, S. B. Tian, C. Z. Gu, Y. G. Shi, Y. F. Guo, Z. G. Cheng, J. P. Hu, L. Zhao, G. H. Yang, E. Sutter, P. Sutter, Y. L. Wang, W. Ji, X. J. Zhou, H. J. Gao, *Nat. Commun.* **2020**, *11*, 2453.
- [28] J. Y. Moon, M. Kim, S. I. Kim, S. Xu, J. H. Choi, D. Whang, K. Watanabe, T. Taniguchi, D. S. Park, J. Seo, S. H. Cho, S. K. Son, J. H. Lee, *Sci. Adv.* **2020**, *6*, eabc6601.
- [29] C. Lee, H. Yan, L. E. Brus, T. F. Heinz, J. Hone, S. Ryu, *ACS Nano* **2010**, *4*, 2695.
- [30] A. Allain, J. Kang, K. Banerjee, A. Kis, *Nat. Mater.* **2015**, *14*, 1195.
- [31] X. Wang, B. Wang, Y. Wu, E. Wang, H. Luo, Y. Sun, D. Fu, Y. Sun, K. Liu, *ACS Appl. Mater. Interfaces* **2021**, *13*, 26143.
- [32] H. M. Khalil, M. F. Khan, J. Eom, H. Noh, *ACS Appl. Mater. Interfaces* **2015**, *7*, 23589.
- [33] X. Cui, G. H. Lee, Y. D. Kim, G. Arefe, P. Y. Huang, C. H. Lee, D. A. Chenet, X. Zhang, L. Wang, F. Ye, F. Pizzocchero, B. S. Jessen, K. Watanabe, T. Taniguchi, D. A. Muller, T. Low, P. Kim, J. Hone, *Nat. Nanotechnol.* **2015**, *10*, 534.
- [34] H. Li, M. Cheng, P. Wang, R. Du, L. Song, J. He, J. Shi, *Adv. Mater.* **2022**, *34*, e2200885.
- [35] A. Daus, S. Vaziri, V. Chen, C. Koroglu, R. W. Grady, C. S. Bailey, H. R. Lee, K. Schauble, K. Brenner, E. Pop, *Nat. Electron.* **2021**, *4*, 495.
- [36] R. Khazaka, L. Mendizabal, D. Henry, R. Hanna, *IEEE Trans. Power Electron.* **2015**, *30*, 2456.
- [37] M. G. Lu, M. J. Shim, S. W. Kim, *J. Appl. Polym. Sci.* **2001**, *81*, 2253.
- [38] D. Lu, C. Wong, *Materials for advanced packaging*, Springer, New York, NY, USA **2009**, Ch. 10.
- [39] J. L. Doherty, S. G. Noyce, Z. Cheng, H. Abuzaid, A. D. Franklin, *ACS Appl. Mater. Interfaces* **2020**, *12*, 35698.
- [40] P. F. Luo, C. Liu, J. Lin, X. P. Duan, W. J. Zhang, C. Ma, Y. W. Lv, X. M. Zou, Y. A. Liu, F. Schwierz, W. J. Qin, L. Liao, J. He, X. Q. Liu, *Nat. Electron.* **2022**, *5*, 849.

This article is protected by copyright. All rights reserved.

- [41] S. Das, A. Sebastian, E. Pop, C. J. McClellan, A. D. Franklin, T. Grasser, T. Knobloch, Y. Illarionov, A. V. Penumatcha, J. Appenzeller, Z. H. Chen, W. J. Zhu, I. Asselberghs, L. J. Li, U. E. Avci, N. Bhat, T. D. Anthopoulos, R. Singh, *Nat. Electron.* **2021**, 4, 786.
- [42] J. Wang, L. Cai, J. Chen, X. Guo, Y. Liu, Z. Ma, Z. Xie, H. Huang, M. Chan, Y. Zhu, L. Liao, Q. Shao, Y. Chai, *Sci. Adv.* **2021**, 7, eabf8744.
- [43] G. Kwon, Y. H. Choi, H. Lee, H. S. Kim, J. Jeong, K. Jeong, M. Baik, H. Kwon, J. Ahn, E. Lee, M. H. Cho, *Nat. Electron.* **2022**, 5, 241.
- [44] H. Qiu, L. J. Pan, Z. N. Yao, J. J. Li, Y. Shi, X. R. Wang, *Appl. Phys. Lett.* **2012**, 100, 123104.
- [45] K. Uchida, A. Ayame, *Surf. Sci.* **1996**, 357, 170.
- [46] A. Ermolieff, P. Bernard, S. Marthon, P. Wittmer, *Surf. Interface Anal.* **1988**, 11, 563.
- [47] D. Gonbeau, C. Guimon, G. Pfisterguillouzo, A. Levasseur, G. Meunier, R. Dormoy, *Surf. Sci.* **1991**, 254, 81.
- [48] Y. Wang, H. Sun, S. Tan, H. Feng, Z. Cheng, J. Zhao, A. Zhao, B. Wang, Y. Luo, J. Yang, J. G. Hou, *Nat. Commun.* **2013**, 4, 2214.
- [49] X. Wang, W. Fan, Z. Fan, W. Dai, K. Zhu, S. Hong, Y. Sun, J. Wu, K. Liu, *Nanoscale* **2018**, 10, 3540.
- [50] W. K. Morrow, S. J. Pearton, F. Ren, *Small* **2016**, 12, 120.
- [51] G. Kresse, *J. Non-Cryst. Solids* **1995**, 193, 222.
- [52] G. Kresse, J. Furthmuller, *Phys. Rev. B* **1996**, 54, 11169.
- [53] J. P. Perdew, K. Burke, M. Ernzerhof, *Phys. Rev. Lett.* **1996**, 77, 3865.
- [54] C. J. Forst, C. R. Ashman, K. Schwarz, P. E. Blochl, *Nature* **2004**, 427, 53.
- [55] S. Grimme, J. Antony, S. Ehrlich, H. Krieg, *J. Chem. Phys.* **2010**, 132, 154104.

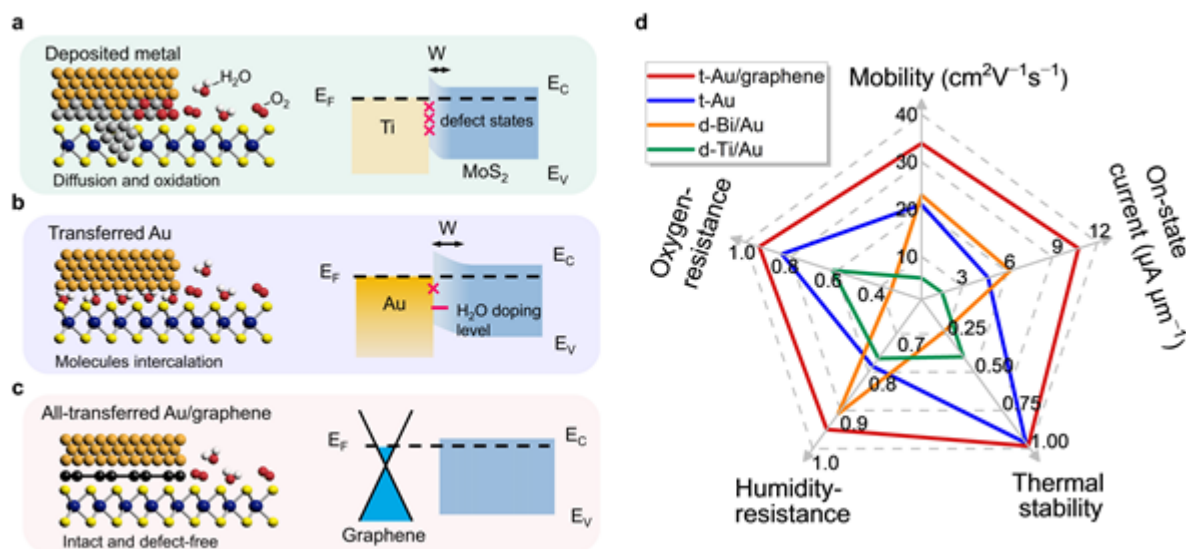


**Figure 1. Atomic structures, band structures, and comprehensive performance for MoS<sub>2</sub> transistors contacted with different kinds of electrodes.** (a) Deposited Ti/Au electrode. (b) Transferred Au electrode. (c) All-transferred Au/graphene electrode. (d) A radar chart comparing the mobility, on-state current, humidity resistance, oxygen resistance, and thermal stability of different kinds of electrodes for MoS<sub>2</sub> transistors. The latter three parameters are estimated by the formula  $1 - |\Delta I_{on}/I_{on}|$ , where  $I_{on}$  is the pristine on-state current and  $\Delta I_{on}$  is the change in  $I_{on}$  when the device is exposed to a humid (RH=100%) or oxidizing environment or after it experiences high-temperature annealing (350 °C). All of the data in (d) are extracted from the experimental results shown in the main text and supplementary information.

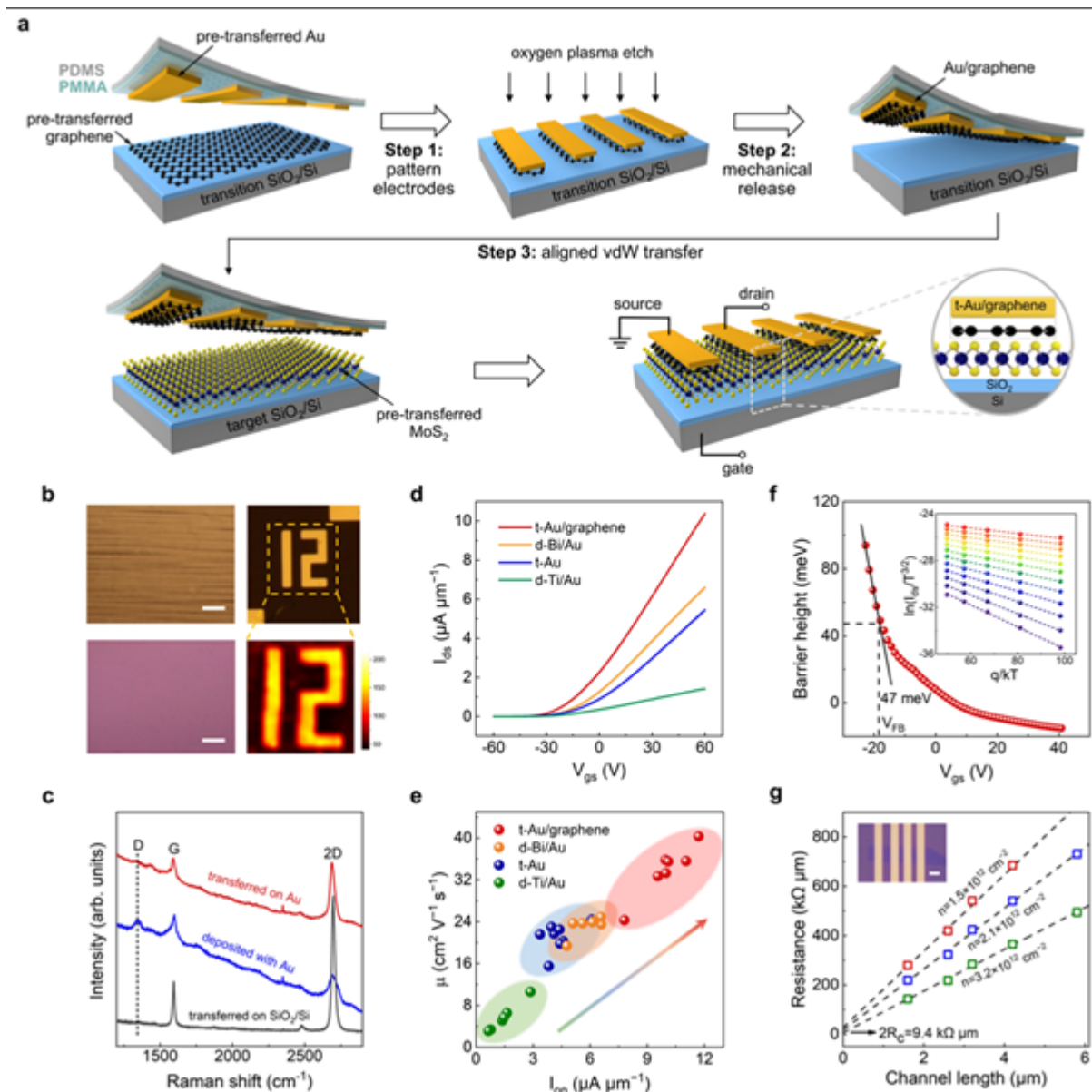


**Figure 2. Characterization and electrical properties of t-Au/graphene-contacted MoS<sub>2</sub> devices.** (a) Schematic diagram of the preparation of t-Au/graphene electrodes with the all-transfer method. (b) Optical images of monolayer graphene grown on a Cu film (top-left), transferred to a SiO<sub>2</sub>/Si substrate (bottom-right), and transferred to Au patterns (top-right). The Raman intensity mapping of the graphene 2D peak at 2697 cm<sup>-1</sup> (bottom-right, on the marking character "12" of Au) indicates the uniform coating of graphene on Au. Scale bar, 50 μm. (c) Raman spectra of monolayer graphene transferred on SiO<sub>2</sub>/Si substrate, transferred on Au, and deposited with Au. (d) Transfer curves of the MoS<sub>2</sub> transistors with different kinds of electrodes at  $V_{ds} = 1$  V. (e) On-state currents and mobilities of

This article is protected by copyright. All rights reserved.

MoS<sub>2</sub> devices with different kinds of electrodes. (f) Barrier heights of t-Au/graphene-contacted MoS<sub>2</sub> transistors as a function of gate voltage. Inset, linear-fitted Arrhenius plots at varied  $V_{gs}$ . (g) Dependence of the overall device resistance (normalized by the channel width) on the channel length under different carrier densities. Inset, optical image of a t-Au/graphene-MoS<sub>2</sub> transistor. Scale bar, 3  $\mu\text{m}$ .

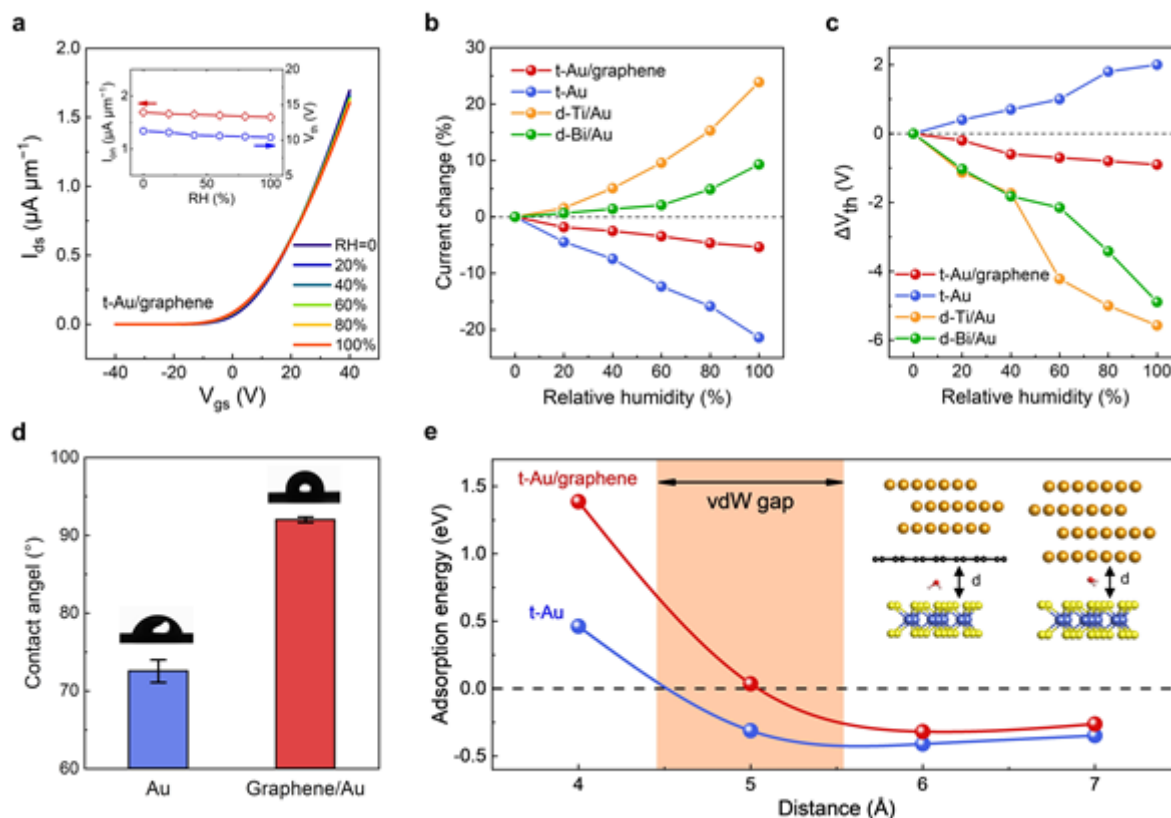


**Figure 3. Humidity-resistance of t-Au/graphene-contacted MoS<sub>2</sub> transistors.** (a) Transfer curves of the t-Au/graphene-contacted MoS<sub>2</sub> device at  $V_{ds} = 0.5$  V under different RHs. Inset, on-state current and threshold voltage as functions of relative humidity. (b) Changes of on-state currents of MoS<sub>2</sub> devices with different electrodes under different RHs. (c) Threshold voltage shift of the MoS<sub>2</sub> FETs with different electrode interfaces under different RHs. (d) Contact angles between water and Au with and without the insertion of monolayer graphene. (e) Calculated adsorption energies of a water molecule between MoS<sub>2</sub> and Au or Au/graphene separated with different distances ( $d$ ) ranging from 4 to 7 Å. Inset, side view of Au/graphene/MoS<sub>2</sub> and Au/MoS<sub>2</sub> configurations with the insertion of a water molecule.

This article is protected by copyright. All rights reserved.

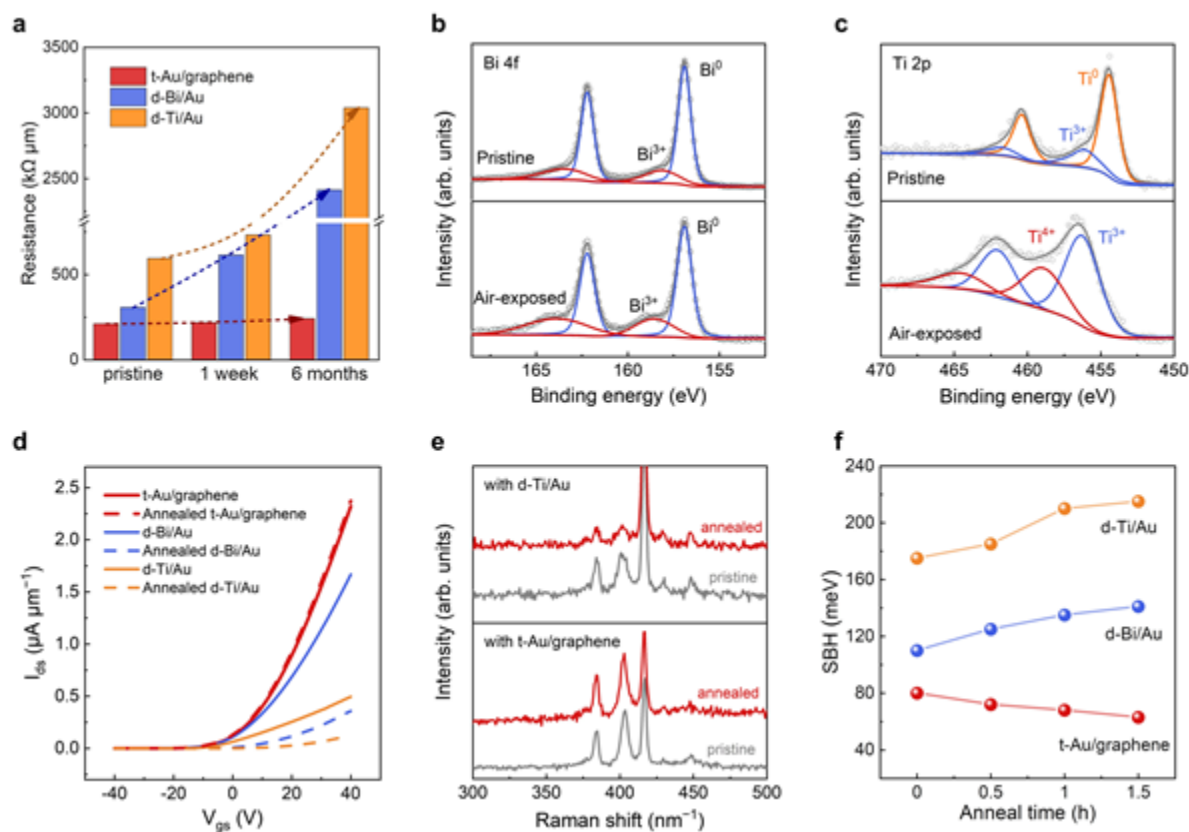


**Figure 4. Stability of t-Au/graphene-contacted MoS<sub>2</sub> devices in an oxidizing environment and at high temperature.** (a) Resistance of MoS<sub>2</sub> devices with different kinds of electrodes as a function of time. During the measurement, the devices were put in a chamber under a total pressure of 10 mbar (80 vol% N<sub>2</sub> and 20 vol% O<sub>2</sub>). (b) Changes in XPS binding energies of Bi for a d-Bi/Au-contacted device, as-prepared and exposed in air for 2 weeks. (c) Changes in XPS binding energies of Ti for a d-Ti/Au-contacted device, as-prepared and exposed in air for 2 weeks. (d) Transfer curves of the MoS<sub>2</sub> devices with different kinds of electrodes before (solid line) and after (dashed line) being annealed at 350 °C in 99.999%-purity Ar. (e) Raman spectra of MoS<sub>2</sub> covered by t-Au/graphene and d-Ti/Au electrodes before and after 350 °C annealing in 99.999%-purity Ar. (f) Evolution of the Schottky barrier height of t-Au/graphene, d-Bi/Au, and d-Ti/Au-contacted devices with annealing time at 350 °C.

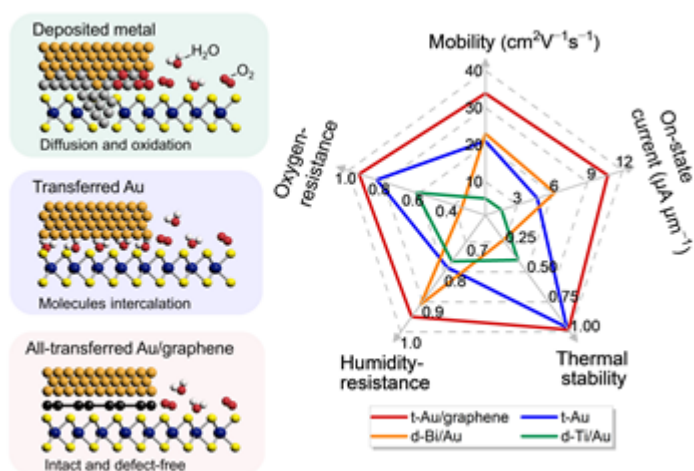
#### Table of contents entry

We demonstrate harsh-environment-resistant MoS<sub>2</sub> field-effect transistors by engineering the electrode-channel interfaces with an all-transfer technique of van der Waals electrodes. The intact

and defect-free interfaces not only reduce the Schottky barrier height at electrodes, but enable high resistances of the MoS<sub>2</sub> devices to humid, oxidizing, and high-temperature environments, surpassing the devices with other kinds of electrodes.

Yonghuang Wu, Zeqin Xin, Zhibin Zhang, Bolun Wang, Ruixuan Peng, Enze Wang, Run Shi, Yiqun Liu, Jing Guo, Kaihui Liu, Kai Liu\*

## All-transfer electrode interface engineering towards harsh-environment-resistant MoS<sub>2</sub> field-effect transistors



This article is protected by copyright. All rights reserved.